# Electrically controlled self-similar evolution of viscous fingering patterns

Pedro H. A. Anjos, Meng Zhao, John Lowengrub, and Shuwang Li

Phys. Rev. Fluids **7**, 053903 — Published 25 May 2022

DOI: 10.1103/PhysRevFluids.7.053903

# Electrically-controlled self-similar evolution of viscous fingering patterns

Pedro H. A. Anjos[1],* Meng Zhao[2],† John Lowengrub[3],‡ and Shuwang Li[1]§

[1]*Department of Applied Mathematics, Illinois Institute of Technology, Chicago, Illinois 60616, USA*

[2] *Center for Mathematical Sciences, Huazhong University of Science and Technology, Wuhan 430074, China*

[3]*Department of Mathematics, University of California at Irvine, Irvine, California 92697, USA*

We design a controlling protocol for the traditional viscous fingering instability by taking advantage of an electro-osmotic flow generated by an external electric field. Under the coupled action of time-varying electric currents and injection rates, fully nonlinear simulations show that, besides setting the number of fingers on the interface, our strategy can either delay or promote the self-similar regime by several orders of magnitude, or even suppress it. In addition, we can produce self-similar shapes ranging from almost circular, mildly perturbed boundaries to fully developed fingered structures with large perturbation amplitudes. All these features are controlled without altering the material properties of the fluids and cell's geometry.

* pamorimanjos@iit.edu (corresponding author)

† mzhao9@hust.edu.cn

‡ lowengrb@math.uci.edu

§ sli@math.iit.edu

These authors contributed equally: Pedro H. A. Anjos, Meng Zhao.

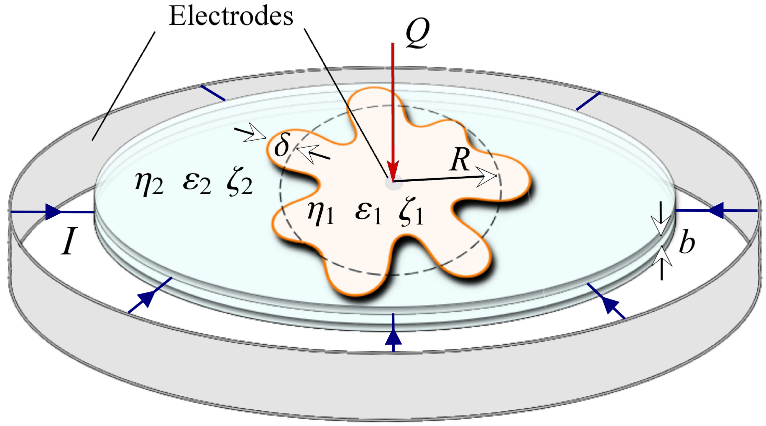


FIG. 1. Representative sketch of the electrohydrodynamic Hele-Shaw flow.

## I. INTRODUCTION

Viscous fingering (or Saffman-Taylor instability) [1] is perhaps the most well-known and studied phenomenon among a family of phenomena that exhibit interfacial instabilities. This hydrodynamic instability arises when a fluid displaces another of higher viscosity in the narrow gap separating two flat, parallel glass plates of an experimental device known as Hele-Shaw cell. The interplay of viscous and surface tension forces is responsible for the formation of highly intricate interfacial patterns [2–5]. Despite the rich dynamical behaviors and eye-catching morphologies, the emergence of intricate patterned structures can be detrimental for some technological and industrial applications [6–10] due to their unpredictable, disordered growth. For instance, processes related to oil recovery [6, 7] by water flooding method are very inefficient if viscous fingering develops at the interface separating the water and oil phases. On the other hand, it is well-known that the emergence of these instabilities enhances fluids mixing [11] and is, therefore, desirable in that case. These facts have stimulated research efforts to develop a fundamental understanding of the interfacial dynamics of these systems and to find ways to control such hydrodynamic instabilities. So, methods aimed toward either suppressing or enhancing fingering instabilities, or prescribing an ordered growth of viscous fingers are of technological and scientific importance.

Several controlling strategies have been developed in the past years, exploiting, for instance, the manipulation of the Hele-Shaw cell geometry [12–17], usage of elastic-walled cells [18], and employment of specific time-dependent injection fluxes [19–29] and gap widths [28, 30–34]. More recently, researchers [35, 36] have achieved interfacial control in Hele-Shaw cells by harnessing electro-osmotic flows generated through externally applied electric fields. Electro-osmotic flow arises over electrically charged surfaces due to the interaction of an externally applied electric field with the net charge in the electric double layer (EDL) [37–39]. In the context of Hele-Shaw flows, when the fluids are brought into contact with the Hele-Shaw cell's glass plates, the glass surface becomes negatively charged due to the dissociation of ionic surface groups. Consequently, a thin, diffuse cloud of excess counter-ions in the liquids accumulate near the surface, forming the so-called EDL. By applying the external electric field, these mobile ions are subjected to a net electric force, which drives an electro-osmotic flow, in addition to the pressure-driven flow. In Refs. [35, 36], the authors demonstrated via linear stability analysis, numerical simulations, and experiments that, depending on the magnitude and direction of the electric current, viscous fingering instabilities can be either enhanced or suppressed.

Here, we further explore the system examined in Refs. [35, 36], but with a different goal in mind: Instead of using electric fields to enhance or suppress interfacial instabilities, we utilize it to promote controlled evolution of an unstable interface and also to tune interesting nonlinear behaviors. More specifically, we design a controlling strategy coupling time-dependent electric currents with time-varying injection rates that can make the interface evolve self-similarly with a fixed number of fingers. This was achieved previously in Refs. [19, 20, 23, 24, 28] by utilizing only a time-dependent injection rate. However, by adding the electro-osmotic contribution to the pressure-driven flow, we demonstrate that the role of fixing the number of fingers can be transferred from the injection rate to the applied electric current. Therefore, the injection rate can vary "freely" (subjected to a given constraint) to tune other features of the flow, such as the establishment of the self-similar regime (delay, promote, or suppress) and the relative finger instability size without altering other physical parameters, including the material properties of the fluids, cell's geometry, and initial conditions.

## II. THEORETICAL BACKGROUND

Consider a radial Hele-Shaw cell (see Fig. 1) of gap thickness $b$ containing two immiscible, incompressible, Newtonian viscous fluids. Denote the viscosities, permittivities, and zeta (surface) potentials of the inner (1) and outer (2) fluids as $\eta_1$, $\varepsilon_1$, $\zeta_1$, and $\eta_2$, $\varepsilon_2$, and $\zeta_2$, respectively, where $\varepsilon_0 \approx 8.85 \times 10^{-12}$ F/m is the vacuum permittivity. At the interfacial boundary where the two fluids meet, there exists a surface tension $\gamma$. The fluid 1 is injected at the center of the cell at a given volumetric injection rate $Q = Q(t)$, displacing the fluid 2 radially. An electric current $I = I(t)$ is applied by electrodes positioned at the center and the outer edge of the Hele-Shaw cell, and an external, in-plane electric field $\mathbf{E}_j = -\boldsymbol{\nabla} V_j$ is established parallel to the flow direction, where $V_j$ is the electric potential in fluid $j$ $(j = 1, 2)$.

By considering the contribution of electric forces, and assuming a thin EDL, the motion of the fluids in the effectively two-dimensional Hele-Shaw cell problem is described by a modified Darcy's law [35, 36, 38, 40] for the gap-averaged velocity $\mathbf{v}_j = -M_j \boldsymbol{\nabla} p_j - K_j \boldsymbol{\nabla} V_j$, where $M_j = b^2/12\eta_j$ and $K_j = -\varepsilon_j \zeta_j/\eta_j$ are the hydraulic and electro-osmotic mobilities, respectively, and $p_j$ represents the pressure. The electric-induced flow can be either in the same or in the opposite direction of hydraulic flow, depending on the direction of the applied electric field, which is related to the sign of the electric current: Positive (negative) current is defined to be in the same (opposite) direction as the flow. We point out that this modified Darcy's law, valid for both hydraulic and electro-osmotic forces, is obtained under traditional Hele-Shaw conditions (i.e., low flow velocities, small gap width, highly viscous displaced fluid, etc.). Furthermore, one must also consider the additional physical requirement of EDL thickness much smaller than gap thickness $b$. Given that the EDL thickness is of the order of the Debye length $\lambda_D \sim 10$ nm $\ll b$ (see Table I), the electro-osmotic mobility $K_j$ is expressed by the Helmholtz-Smoluchowski relation [38]. Thus Darcy's law (total gap-averaged velocity) is written as the sum of gap-averaged hydraulic and electro-osmotic velocities, with $K_j = -\varepsilon_j \zeta_j/\eta_j$.

As the electric field acts on the EDL to promote electro-osmotic flow, pressure gradients also drive the advection of ions on the EDL, generating a streaming current. As a consequence, the total current density $\mathbf{J}_j$ is the sum of streaming (pressure-induced) and Ohmic (associated with the electric field) currents, i.e., $\mathbf{J}_j = -K_j \boldsymbol{\nabla} p_j - \sigma_j \boldsymbol{\nabla} V_j$, where $\sigma_j$ is the Ohmic conductivity of fluid $j$.

The interface motion is determined by the previous governing equations (for $\mathbf{v}_j$ and $\mathbf{J}_j$), along with the incompressibility $\boldsymbol{\nabla} \cdot \mathbf{v}_j = 0$ and continuity $\boldsymbol{\nabla} \cdot \mathbf{J}_j = 0$ conditions, and four boundary conditions at the fluid-fluid interface. The first one expresses the pressure discontinuity due to the interfacial surface tension $\gamma$, and it is given by the Young-Laplace [1, 3–5] pressure boundary condition $p_1 - p_2 = \gamma\kappa$, where $\kappa$ denotes the curvature of the fluid-fluid interface. Conversely, the electric potential is continuous across the interface [35, 36, 40], i.e., $V_1 - V_2 = 0$. The other two remaining fluid-fluid conditions are the kinematic boundary conditions [1, 3–5, 35, 36, 40], which express the fact that the normal components of the fluids' velocities and also of the current densities are continuous across the interface. These conditions are expressed as $\mathbf{v}_1 \cdot \hat{\mathbf{n}} = \mathbf{v}_2 \cdot \hat{\mathbf{n}}$ and $\mathbf{J}_1 \cdot \hat{\mathbf{n}} = \mathbf{J}_2 \cdot \hat{\mathbf{n}}$, where $\hat{\mathbf{n}}$ denotes the unit normal vector at the interface.

Although the results depicted in Figs. 2 – 6 are obtained utilizing fully nonlinear simulations, our controlling protocol, the main result of this work, is derived from linear theory. Linear stability analysis of the problem [35] considers harmonic distortions of a nearly circular fluid-fluid interface whose position evolves according to $\mathcal{R}(\theta, t) = R(t) + \delta(\theta, t)$, where $R = R(t)$ is the time-dependent unperturbed radius of the interface, and $\theta$ denotes the azimuthal angle in the $r - \theta$ plane. The unperturbed radius of the interface at $t = 0$ is denoted by $R(t = 0) = R_0$, and the net interface disturbance is represented as a Fourier series $\delta(\theta, t) = \sum_{n=-\infty}^{+\infty} \delta_n(t)\ e^{in\theta}$, where $\delta_n(t)$ denotes the complex Fourier amplitudes, with integer wave numbers $n$, and $|\delta| \ll R$. Utilizing the governing equations and also the boundary conditions of the problem, we obtain the equation of motion $\dot{\delta}_n = \lambda(n)\delta_n$ (for $n \neq 0$) for the perturbation amplitudes, where

$$\lambda(n) = \frac{Q}{2\pi b R^2}(A|n| - 1) - \frac{\gamma}{R^3} B|n|(n^2 - 1) + \frac{I}{\pi b R^2} C|n| \tag{1}$$

is the linear growth rate, with electro-osmotic viscosity contrast

$$A = \frac{K_1^2 - K_2^2 - (\sigma_1 + \sigma_2)(M_1 - M_2)}{(K_1 + K_2)^2 - (\sigma_1 + \sigma_2)(M_1 + M_2)}. \tag{2}$$

Additionally,

$$B = \frac{M_1 K_2^2 + M_2 K_1^2 - (\sigma_1 + \sigma_2) M_1 M_2}{(K_1 + K_2)^2 - (\sigma_1 + \sigma_2)(M_1 + M_2)}, \tag{3}$$

and

$$C = \frac{M_1 K_2 - M_2 K_1}{(K_1 + K_2)^2 - (\sigma_1 + \sigma_2)(M_1 + M_2)}. \tag{4}$$

The first term appearing on the right-hand side of Eq. (1) represents the destabilizing contribution (for $A > 0$) coming from the radial injection of the inner fluid, while the second term accounts for the stabilizing effect due to the surface tension. Supplementing these usual terms related to injection-driven Hele-Shaw flows, there is also an additional term proportional to $IC$, which arises as a consequence of the consideration of the electro-osmotic flow. This new term can promote linear stabilization ($IC < 0$) or destabilization ($IC > 0$) depending on its sign. In addition, note that at the linear level electro-osmotic effects also modify the parameters $A$ and $B$, which, in the absence of electro-osmotic effects ($K_1 = K_2 = 0$), are given by $A = (\eta_2 - \eta_1)/(\eta_2 + \eta_1)$ and $B = b^2/[12(\eta_1 + \eta_2)]$, respectively.

## III. CONTROLLING PROTOCOL

In contrast to what has been employed in Refs. [35, 36], instead of utilizing constant values for $Q$ and $I$, which may result in finger proliferation, here we consider that both quantities may be functions of time, i.e., $Q = Q(t)$ and $I = I(t)$. At the linear level, an estimate for the number of fingers formed during the injection process is given by the closest integer to the mode of largest growth rate $n_{\rm max}$ [2–5], found by evaluating $d\lambda/dn|_{n=n_{\rm max}} = 0$. Since we intend to keep this number fixed, our job is to determine the functional forms of $Q(t)$ and $I(t)$ that keep $n_{\rm max}$ unmodified as the interface evolves. Considering Eq. (1), $d\lambda/dn|_{n=n_{\rm max}} = 0$ is easily evaluated. Then, by solving the resulting expression for $I(t)$, we obtain

$$I(t) = \frac{1}{C}\left[\frac{\pi b\gamma B}{R(t)}(3n_{\rm max}^2 - 1) - \frac{Q(t)A}{2}\right]. \tag{5}$$

Note that it does not impose any restrictions on the functional form and values of the injection rate $Q(t)$. Therefore, *a priori*, any $Q(t)$, including constant values, could be utilized to keep $n_{\rm max}$ unmodified as long as $I(t)$ varies in time accordingly to Eq. (5). However, this is not true, and we address this point in the following calculations.

By inserting Eq. (5) into Eq. (1), and evaluating the resulting expression at $n = n_{\rm max}$, we obtain the growth rate $\lambda(n_{\rm max}) = \frac{1}{R^3(t)}\left[2\gamma B n_{\rm max}^3 - \frac{Q(t)R(t)}{2\pi b}\right]$. Note that if one assumes that the injection process is performed under constant rate, i.e., $Q(t) = Q_0$, the second term inside the squared brackets dominates for larger interfacial sizes [$R(t)$], and $n_{\rm max}$ becomes a stable mode [$\lambda(n_{\rm max}) < 0$]. Recall that $n_{\rm max}$ is the mode of largest growth rate, so when it becomes a stable mode, all the other modes in the dynamics become stable as well. Consequently, the interface expands as a stable circle and not as a controlled boundary with a specific number of fingers, as we would like. Therefore, to control the shape of the interface during injection-driven, electro-osmotic flows, one must consider not only a time-dependent electric current [Eq. (5)], but also a time-dependent injection rate. Moreover, in order to guarantee that $n_{\rm max}$ is an unstable mode during all the injection process, and to ensure the formation of fingered structures, we need that $\lambda(n_{\rm max}) > 0$, leading to the requirement

$$Q(t) < Q_{\rm crit}(t) = \frac{4\pi b\gamma B n_{\rm max}^3}{R(t)}, \tag{6}$$

where $Q_{\rm crit}(t)$ is the critical injection rate at which $n_{\rm max}$ becomes stable [i.e., $\lambda(n_{\rm max}) = 0$].

Expressions (5) and (6) constitute the central analytical results of this work. Based on the previous calculations and discussions, it is clear that if one intends to control the shape of the expanding interface during injection-driven, electro-osmotic flows, one can consider the controlling electric current (5) and perform the injection process under a positive, time-dependent, non-zero injection rate $Q(t) = \alpha Q_{\rm crit}(t)$, with $0 < \alpha < 1$. Note that volume conservation implies in the relation $Q(t) = 2\pi bR\dot{R}$. Since here we utilize $Q(t) = \alpha Q_{\rm crit}(t)$, $R(t)$ can be easily determined, and once this is done one concludes that $Q(t) \sim t^{-1/3}$.

We also point to the fact that only the controlling electric current (5) depends on $n_{\rm max}$, and on the physical parameters of the system, while $Q(t)$ can be arbitrarily chosen [as long as condition (6) is satisfied] to control other features of the interface and tune dynamical regimes, without the necessity of changing the set of physical parameters, initial conditions or number of fingers. We stress that these controlling features are not possible in the purely hydrodynamic problem. When electro-osmotic effects are absent, i.e., $I(t) = 0$ and $K_1 = K_2 = 0$, Eq. (5) reduces to $Q(t) \equiv Q_{\rm ph}(t) = 2\pi b\gamma B(3n_{\rm max}^3 - 1)/AR(t)$, which is the controlling injection rate for the pure hydrodynamic problem [19, 20]. In this case, if one intends to induce dynamical responses of the interface by manipulating the injection $Q_{\rm ph}(t)$ while keeping the number of fingers fixed ($n_{\rm max}$), then one necessarily has to modify the physical parameters. Likewise, if the physical parameters are kept unaltered but $Q_{\rm ph}(t)$ is adjusted to tune dynamical behaviors, then $n_{\rm max}$ has to change, impacting the interfacial symmetry. All of these problems are eliminated by our new controlling protocol.

| Physical parameter | Value | Units |
|---|---|---|
| $b$ | $10^{-4}$ | m |
| $\varepsilon_0$ | $\approx 8.85 \times 10^{-12}$ | F/m |
| $\eta_1$ | $7.36 \times 10^{-3}$ | Pa s |
| $\varepsilon_1$ | $10.3\varepsilon_0$ | F/m |
| $\zeta_1$ | 0 | V |
| $\eta_2$ | $109 \times 10^{-3}$ | Pa s |
| $\varepsilon_2$ | $49.1\varepsilon_0$ | F/m |
| $\zeta_2$ | $-150 \times 10^{-3}$ | V |
| $\gamma$ | $37 \times 10^{-3}$ | N/m |
| $\sigma_1$, $\sigma_2$ | $155 \times 10^{-4}$ | S/m |
| $R_0$ | $10^{-2}$ | m |
| $A$ | $\approx 0.87$ | – |
| $B$ | $\approx 7.16 \times 10^{-9}$ | $m^4$ $N^{-1}$ $s^{-1}$ |
| $C$ | $\approx -1.80 \times 10^{-8}$ | $m^3$ $A^{-1}$ $s^{-1}$ |

TABLE I. Values of the physical parameters utilized in the simulations depicted in Figs. 2 and 3. The material properties of fluid 1 correspond to the oil 1-octanol with tetrabutyl-ammonium chloride (TBACl) to tune its conductivity. The concentration of TBACl is 0.75 M. Likewise, fluid 2 corresponds to a mixture of water/glycerol (60/40 w/w) with KCl in concentrations $\leq 2 \times 10^{-3}$ M.

## IV. CONTROLLING THE SELF-SIMILAR PATTERNS

In the framework of pure hydrodynamic, injection-driven radial Hele-Shaw flows, it has been demonstrated by fully nonlinear simulations [19, 28] that flows performed under time-dependent injection fluxes scaling as $Q(t) \sim t^{-1/3}$, such as the injection rates utilized in this work, evolve to a self-similar regime characterized by the emergence of radially growing $n$-fold symmetric structures with preserved shapes. Since in our controlling protocol $Q(t)$ can be arbitrarily chosen [obeying condition (6)], we investigate its effects (if any) in the establishment of the self-similar regime, and in the associated pattern morphologies, by utilizing our boundary integral formulation [41–43] (see Appendix A). To strengthen the relevance of our theoretical results, in the remainder of this paper, the values of the parameters (see Table I) used in our simulations (Figs. 2 – 6) are based on the values of the physical quantities utilized in the experimental paper [36] related to injection-driven, electro-osmotic flows in a radial Hele-Shaw cell. In addition, we consider that at $t = 0$ the initial interfacial shape is given by a mode mixture of sines and cosines with all the participating modes having the same initial amplitude ($R_0/100$), i.e., $\mathcal{R}(\theta, 0) = R_0 + R_0/100[\sin(2\theta) + \cos(3\theta) + \sin(5\theta) + \cos(7\theta)]$.

A convenient way to investigate these intrinsically fully nonlinear concerns is through the time evolution of the interfacial shape factor $\Delta(t)/R(t) \equiv \max|\mathcal{R}(\theta, t)/R(t) - 1|$ [19], which is computed numerically based on the maximum deviation of the perturbed interface from the equivalent circle with the same area. In the left panel of Fig. 2, we present the behavior of the shape factor $\Delta(t)/R(t)$ with respect to variations in the ratio $R(t)/R_0$ for thirteen different injection rates. The solid curves correspond to injection-driven, electro-osmotic flows performed utilizing the controlling current (5) with $n_{\max} = 7$ and injection rates $Q(t) = \alpha Q_{\rm crit}(t)$. On the other hand, the dashed curve represents the pure hydrodynamic flow performed using $Q(t) = Q_{\rm ph}(t)$. In addition, in the right panel of Fig. 2, which will be analyzed later together with Fig. 3, we depict the electric current (5) as a function of $R(t)/R_0$ for the injection rates utilized in the left panel.

By following the behavior of the curves in the left panel of Fig. 2, initially, one observes the growth of $\Delta(t)/R(t)$, indicating the regime in which the interface changes its morphology while it expands radially. Nonetheless, as time advances and the interface acquires large sizes, fully nonlinear effects dominate, making most of the curves saturate. Small dots indicate the moment of saturation. From these points onward, the corresponding interfaces evolve self-similarly, keeping a constant interfacial shape profile. We emphasize that this does not mean that the system reaches a stationary state since the interfaces are still expanding radially. Note that although the curve associated with $\alpha = 0.49$ reaches the self-similar regime, it occurs for a very large interfacial size ($R/R_0 = 10^{36}$), and the small dot lies outside the plot interval. On the other hand, the cases with $\alpha = 0.1$ and $\alpha = 0.21$ do not achieve the self-similar regime, and the reason behind this failure in reaching such regime will be provided later when analyzing Fig. 3.

A dynamical behavior revealed by the left panel of Fig. 2 concerns the possibility of tuning the occurrence of the self-similar regime by varying the injection rate. We observe that by properly manipulating $Q(t)$ (or, equivalently, the values of $\alpha$) and the electric current accordingly to Eq. (5), one can tune the establishment of the self-similar regime

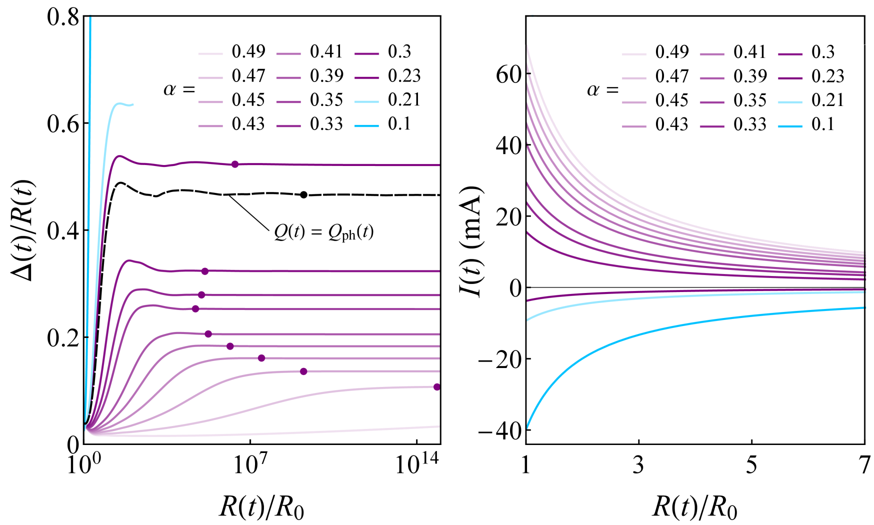


FIG. 2. Left panel: Behavior of the shape factor $\Delta(t)/R(t)$ with respect to variations in the ratio $R(t)/R_0$, for flows performed utilizing the controlling protocol with $n_{\max} = 7$ and various injection rates $Q(t) = \alpha Q_{\rm crit}(t)$. Right panel: Plot of the electric current (5) as a function of $R(t)/R_0$ for the injection rates utilized in the left panel.

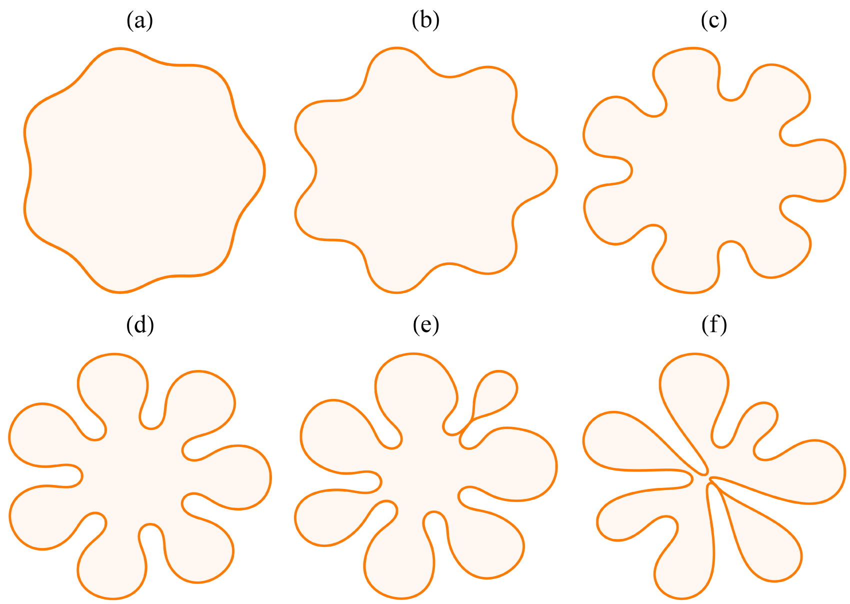


FIG. 3. Gallery of representative fully nonlinear 7-fold patterns (see supplemental material) [44] corresponding to the cases with (a) $\alpha = 0.49$, (b) $\alpha = 0.45$, (c) $\alpha = 0.3$, (d) $\alpha = 0.23$, (e) $\alpha = 0.21$, and (f) $\alpha = 0.1$, shown in Fig. 2. The interfaces (a)-(d) are plotted at the onset of the self-similar regime, i.e., for (a) $R/R_0 = 10^{36}$, (b) $R/R_0 = 1.75 \times 10^9$, (c) $R/R_0 = 1.25 \times 10^5$, and (d) $R/R_0 = 2.29 \times 10^6$. The patterns depicted in (e) and (f) do not reach the self-similar regime, and are plotted for (e) $R/R_0 = 114$ and (f) $R/R_0 = 1.97$.

to occur at interfacial sizes as large as $R/R_0 = 10^{36}$ (for $\alpha = 0.49$), or as small as $R/R_0 = 5.02 \times 10^4$ (for $\alpha = 0.35$). In addition, by utilizing $\alpha \leq 0.21$, one can even stop the occurrence of self-similarity. These novel controlling features are only possible due to the inclusion of the electro-osmotic flow in addition to the usual pressure-driven flow. To make this point very clear, in Fig. 2 we also depict the evolution of the shape factor during a purely hydrodynamic flow performed employing $Q(t) = Q_{\rm ph}(t)$. Although in this case, one also observes establishment of self-similar evolution at $R/R_0 = 1.77 \times 10^9$, there are no ways of tuning its occurrence (delaying, promoting, or suppressing) without modifying $n_{\max}$, the physical parameters, or the initial conditions of the flow. In particular, we point out that, comparing the curve related to $\alpha = 0.35$ with the one associated with $Q(t) = Q_{\rm ph}(t)$, our controlling scheme has promoted the establishment of self-similar evolution by reducing the required interfacial size $R/R_0$ in about 5 orders

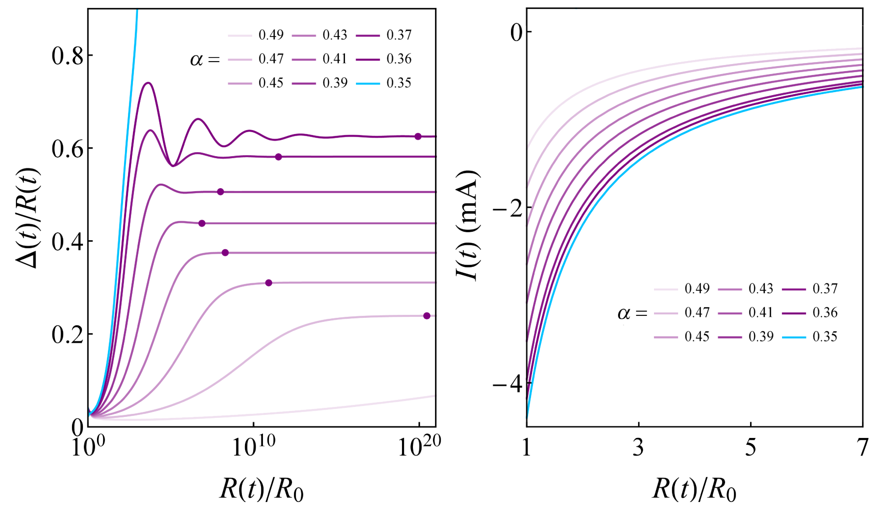


FIG. 4. Left panel: Behavior of the shape factor $\Delta(t)/R(t)$ with respect to variations in the ratio $R(t)/R_0$, for flows performed utilizing the controlling protocol with $n_{\max} = 3$ and various injection rates $Q(t) = \alpha Q_{\text{crit}}(t)$. Right panel: Plot of the electric current (5) as a function of $R(t)/R_0$ for the injection rates utilized in the left panel.

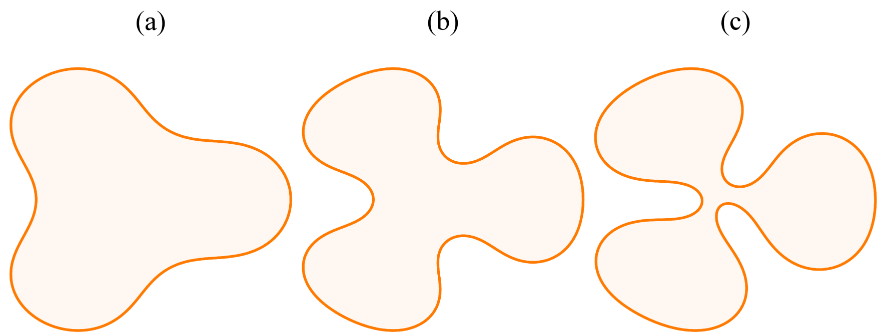


FIG. 5. Gallery of representative fully nonlinear 3-fold patterns corresponding to the cases (a) $\alpha = 0.45$, (b) $\alpha = 0.37$, and (c) $\alpha = 0.35$, shown in Fig. 4. The interfaces (a) and (b) are plotted at the onset of the self-similar regime, i.e., for (a) $R/R_0 = 8.2 \times 10^{10}$ and (b) $R/R_0 = 3.2 \times 10^{11}$. The pattern depicted in (c) does not reach the self-similar regime, and is plotted for $R/R_0 = 1.06 \times 10^3$.

of magnitude with respect to the equivalent purely hydrodynamic case.

In addition to the manipulation of the self-similar dynamics, the analysis of the left panel of Fig. 2 also reveals another interesting fully nonlinear dynamical response of the system to variations in the injection rates employed, namely, for a given value of $R(t)/R_0$, the magnitude of $\Delta(t)/R(t)$ is larger for smaller values of $\alpha$, indicating that the injection rate can also be used to set the instability level of the self-similar shapes. Complementary information about this relevant controlling feature is provided in Fig. 3, where we plot the fully nonlinear patterns related to some of the cases presented in Fig. 2.

By inspecting the panels of Fig. 3, one immediately notes that all the fingered structures are 7-fold, confirming the efficiency of our method to control the number of emerging fingers even at the fully nonlinear regime of the dynamics. Moreover, it is evident that lower injection rates indeed lead to the formation of more disturbed patterns. Therefore, by just adjusting the values of $\alpha$ and keeping all the other physical parameters unchanged, one can generate self-similar patterns with considerably different relative finger sizes, ranging from almost circular, mildly perturbed boundaries [Fig. 3(a)] to fully developed fingered structures with large perturbation amplitudes [Fig. 3(d)]. Nevertheless, if one continues to reduce $\alpha$, the interface becomes increasingly unstable, and we observe a morphological transition from 7-fold, symmetric, self-similar patterns [panels (a)-(d)], to asymmetric 7-finger structures [panels (e) and (f)]. This is clearly illustrated in Fig. 3(e), where we observe the formation of an almost symmetric pattern that seems to evolve towards self-similarity, but this evolution is interrupted due to the occurrence of a pinch-off event. Therefore, the presence of pinch-off events is the cause of the suppression of self-similar evolution discussed in Fig. 2. Finally, in Fig. 3(f), we observe the emergence of an asymmetric, intricate fingered shape dominated by electric-induced pinch-

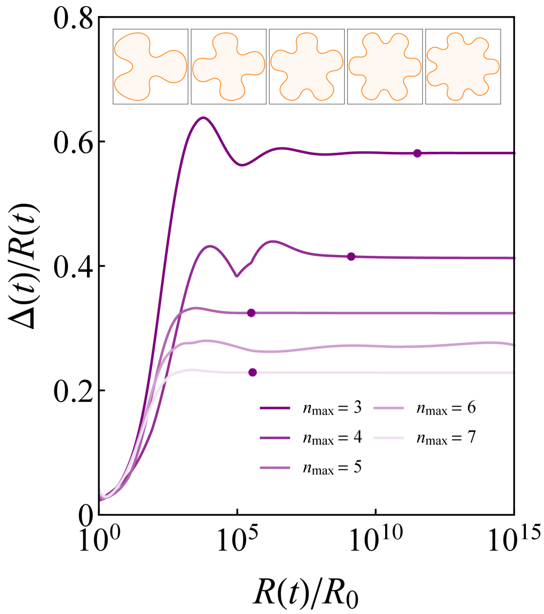


FIG. 6. Behavior of the shape factor $\Delta(t)/R(t)$ with respect to variations in the ratio $R(t)/R_0$, for flows performed utilizing the controlling protocol with $n_{\max} = 3, 4, 5, 6$, and 7. Here $Q(t) = 0.37 \times Q_{\rm crit}(t)$, where $Q_{\rm crit}(t)$ is evaluated for each mode $n_{\max}$ utilizing Eq. 6. The resulting self-similar shapes are depicted as insets.

off instabilities with no resemblance to the well-behaved symmetric patterns depicted in the other panels for larger values of $\alpha$. This morphological transition is explained by inspecting the right panel of Fig. 2: As $\alpha$ is reduced, one diminishes the destabilizing viscous effects but also restrain the stabilization provided by positive electric currents. When the electric current is negative, the electric field turns a destabilizing effect, ultimately leading to pinch-off phenomena for sufficiently large values.

In Figs. 4 – 6, we show that the dynamical behaviors found in our work are general, in the sense that if one selects other modes $n_{\max}$ (for instance, 3, 4, 5, or 6), the key conclusions remain qualitatively the same to the results currently presented in Figs. 2 and 3 for $n_{\max} = 7$, thus supporting the main findings of this work. In addition, we emphasize that we have performed repeated and careful computations utilizing other general initial conditions and checked that the resulting findings are very similar to the ones depicted in Figs. 2 – 6. And finally, in Appendix B, we extend the linear theory derived in Sec. II to a weakly nonlinear theory. Then, we utilize it to strengthen the main findings presented in Sec. IV.

## V. CONCLUSION

Above we show through numerical simulations that dynamical control of fingering instabilities is attained by properly adjusting both electric current and flow rate over time. Our controlling protocol differs from previous strategies performed under time-varying flow rates because of the inclusion of a secondary electro-osmotic flow, which can oppose or assist the pressure-driven flow. Remarkably, this simple modification has provided an improved control over the features and behaviors of the unstable viscous fingering interface. More specifically, we are able to (i) set the number of fingers emerging at the interface, (ii) tune the relative finger instability size of the patterns, and (iii) delay, promote, or suppress the self-similar growth. We stress that all these features are conveniently controlled without altering the material properties of the fluids, cell's geometry, or initial conditions, something impossible to be realized by utilizing conventional strategies performed solely in terms of time-varying flow rates [19, 20, 23, 24, 28].

Many extensions of our work are possible. Although we demonstrate improved interfacial control by utilizing electric fields, our method is general and can be applied to other systems where multiple forces drive interfacial instabilities. For instance, one could use our discoveries to control the features of a radially evolving interface by applying magnetic fields instead of electric fields. In that case, the fluids are magnetic and respond promptly to applied magnetic fields [45–55]. Furthermore, given the existing types of magnetic fluids (ferrofluids and magnetorheological) [45] and the different possibilities of magnetic field arrangements [45–55], these systems could potentially exhibit new dynamical behaviors beyond the ones already disclosed here when controlled by employing our protocol. Therefore, our present study paves the way for other explorations concerning controlling methods exploiting the rich physics behind "multi-field" driven interfacial dynamics.

## ACKNOWLEDGMENTS

P. A. acknowledges useful discussion with José Miranda, Eduardo Dias, and Írio Coutinho. S. L. acknowledges the support from the National Science Foundation, Division of Mathematical Sciences grant DMS-1720420. J. L. acknowledges partial support from the NSF through grants DMS-1714973, DMS-1719960, DMS-1763272, and the Simons Foundation (594598QN) for a NSF-Simons Center for Multiscale Cell Fate Research. J. L. also thanks the National Institutes of Health for partial support through grants 1U54CA217378-01A1 for a National Center in Cancer Systems Biology at UC Irvine and P30CA062203 for the Chao Family Comprehensive Cancer Center at UC Irvine.

## Appendix A: Fully nonlinear boundary integral method

In the advanced-time regime of the dynamics, where the viscous fingering instabilities are comparable to the interfacial radius (as in Figs. 2 – 6), the time evolution of the fluid-fluid boundary can only be appropriately described by fully nonlinear computational methods such as the boundary integral scheme presented in this Appendix. According to potential theory [56], the solution of Laplace's equation can be written in terms of boundary integrals. Since the velocity $\phi_j$ and current density $\psi_j$ potentials obey Laplace's equation and have continuous normal derivatives across the interface (expressed by the kinematic boundary conditions $\mathbf{v}_1 \cdot \hat{\mathbf{n}} = \mathbf{v}_2 \cdot \hat{\mathbf{n}}$ and $\mathbf{J}_1 \cdot \hat{\mathbf{n}} = \mathbf{J}_2 \cdot \hat{\mathbf{n}}$), these two harmonic functions can be constructed as double layer potentials

$$\phi(\mathbf{x}) = \frac{1}{2\pi} \int \mu_1(\mathbf{y}) \frac{\partial \ln|\mathbf{x}-\mathbf{y}|}{\partial \mathbf{n}(\mathbf{y})} ds(\mathbf{y}) + \frac{Q}{2\pi b} \ln|\mathbf{x}|, \tag{A1}$$

and

$$\psi(\mathbf{x}) = \frac{1}{2\pi} \int \mu_2(\mathbf{y}) \frac{\partial \ln|\mathbf{x}-\mathbf{y}|}{\partial \mathbf{n}(\mathbf{y})} ds(\mathbf{y}) + \frac{I}{2\pi b} \ln|\mathbf{x}|, \tag{A2}$$

respectively, where $\mu_1(\mathbf{y})$ and $\mu_2(\mathbf{y})$ are dipole densities on the interface, $s$ denotes the interface arclength, and $\mathbf{x}$ represents the position vector with the origin located at the center of the cell. Note that the kinematic boundary conditions are automatically satisfied by these potentials. Now, we rewrite the right-hand sides of the modified Darcy's law and the equation for the total current density in terms of the double layer potentials (A1) and (A2), and substitute the resulting expressions in the remaining boundary conditions for the pressure and electric potential to obtain the integral equations

$$\begin{aligned} &\left(\frac{\sigma_1}{H_1} + \frac{\sigma_2}{H_2}\right) \mu_1(\mathbf{x}) + \frac{1}{\pi}\left(\frac{\sigma_1}{H_1} - \frac{\sigma_2}{H_2}\right) \int \mu_1(\mathbf{y}) \frac{\partial \ln|\mathbf{x}-\mathbf{y}|}{\partial \mathbf{n}(\mathbf{y})} ds(\mathbf{y}) \\ &- \left(\frac{K_1}{H_1} + \frac{K_2}{H_2}\right) \mu_2(\mathbf{x}) - \frac{1}{\pi}\left(\frac{K_1}{H_1} - \frac{K_2}{H_2}\right) \int \mu_2(\mathbf{y}) \frac{\partial \ln|\mathbf{x}-\mathbf{y}|}{\partial \mathbf{n}(\mathbf{y})} ds(\mathbf{y}) \\ &= 2\gamma\kappa - \left(\frac{\sigma_1}{H_1} - \frac{\sigma_2}{H_2}\right) \frac{Q}{2\pi b} \ln|\mathbf{x}|^2 + \left(\frac{K_1}{H_1} - \frac{K_2}{H_2}\right) \frac{I}{2\pi b} \ln|\mathbf{x}|^2, \end{aligned} \tag{A3}$$

and

$$\begin{aligned} &- \left(\frac{K_1}{H_1} + \frac{K_2}{H_2}\right) \mu_1(\mathbf{x}) - \frac{1}{\pi}\left(\frac{K_1}{H_1} - \frac{K_2}{H_2}\right) \int \mu_1(\mathbf{y}) \frac{\partial \ln|\mathbf{x}-\mathbf{y}|}{\partial \mathbf{n}(\mathbf{y})} ds(\mathbf{y}) \\ &+ \left(\frac{M_1}{H_1} + \frac{M_2}{H_2}\right) \mu_2(\mathbf{x}) + \frac{1}{\pi}\left(\frac{M_1}{H_1} - \frac{M_2}{H_2}\right) \int \mu_2(\mathbf{y}) \frac{\partial \ln|\mathbf{x}-\mathbf{y}|}{\partial \mathbf{n}(\mathbf{y})} ds(\mathbf{y}) \\ &= \left(\frac{K_1}{H_1} - \frac{K_2}{H_2}\right) \frac{Q}{2\pi b} \ln|\mathbf{x}|^2 - \left(\frac{M_1}{H_1} - \frac{M_2}{H_2}\right) \frac{I}{2\pi b} \ln|\mathbf{x}|^2, \end{aligned} \tag{A4}$$

where $H_j = \sigma_j M_j - K_j^2$ (with $j = 1, 2$). These equations form a system of well-defined Fredholms integral equations of the second kind, and we solve it for the dipole densities $\mu_1(\mathbf{x})$ and $\mu_2(\mathbf{x})$ via the iterative method GMRES [57]. Once $\mu_1(\mathbf{x})$ and $\mu_2(\mathbf{x})$ are solved, we compute the normal velocity of the interface via Dirichlet-Neumann mapping [58]

$$V(t) = \frac{1}{2\pi} \int \mu_{1s'} \frac{(\mathbf{x}-\mathbf{x}')^{\perp} \cdot \mathbf{n}(\mathbf{x})}{|\mathbf{x}-\mathbf{x}'|^2} ds'(\mathbf{x}') + \frac{Q}{2\pi b} \frac{\mathbf{x} \cdot \mathbf{n}}{|\mathbf{x}|^2}, \tag{A5}$$

where the subscript $s'$ denotes the partial derivative with respect to arclength and $\mathbf{x}^{\perp} = (x_2, -x_1)$. Finally, the interface is evolved through

$$\frac{d\mathbf{x}}{dt} \cdot \mathbf{n} = V. \tag{A6}$$

Note that in Eq. (A5), the normal velocity decreases as the interface size $|\mathbf{x}|$ gets large. It prohibits one from computing the dynamics of an interface at very long times. Thus, we apply the rescaling idea [33, 34, 41, 42] to accelerate this slow dynamics. We first introduce

$$\mathbf{x} = \bar{R}(\bar{t})\bar{\mathbf{x}}(\bar{t}, \theta), \tag{A7}$$

and

$$\bar{t} = \int_0^t \frac{1}{\rho(t')} dt', \tag{A8}$$

where the space scaling $\bar{R}(\bar{t})$ represents the size of the interface, $\bar{\mathbf{x}}$ is the position vector in the scaled interface, and $\theta$ parameterizes the interface. The time scaling function $\rho(t) = \bar{\rho}(\bar{t})$ maps the original time $t$ to the new time $\bar{t}$. In addition, note that $\rho(t)$ has to be positive and continuous. The evolution of the interface in the scaled frame can be accelerated [41, 42] or decelerated [33, 34] by choosing differents $\rho(t)$. A straightforward calculation shows that the normal velocity in the new frame is expressed as

$$\bar{V}(\bar{t}) = \frac{\bar{\rho}}{\bar{R}} V(t(\bar{t})) - \frac{\bar{\mathbf{x}} \cdot \mathbf{n}}{\bar{R}} \frac{d\bar{R}}{d\bar{t}}. \tag{A9}$$

In the rescaled frame, we require that the area enclosed by the interface remains constant $\bar{A}(\bar{t}) = \bar{A}(0)$. Thus, the integration of the normal velocity along the interface in the scaled frame vanishes, i.e., $\int_{\bar{\Gamma}(\bar{t})} \bar{V} d\bar{s} = 0$. As a consequence,

$$\frac{d\bar{R}}{d\bar{t}} = \frac{\bar{\rho}\bar{Q}}{2b\bar{A}(0)\bar{R}}. \tag{A10}$$

By choosing $\rho(\bar{t}) = \bar{R}^2(\bar{t})$, the interface grows exponentially in the rescaled frame as

$$\bar{R}(\bar{t}) = \exp\left[\frac{\bar{Q}}{2b\bar{A}(0)}\bar{t}\right]. \tag{A11}$$

Taking $\bar{\mu}_1(\bar{\mathbf{x}}) = \mu_1(\mathbf{x})\bar{R}(\bar{t})$ and $\bar{\mu}_2(\bar{\mathbf{x}}) = \mu_2(\mathbf{x})\bar{R}(\bar{t})$, we rewrite the integral equations (A3) and (A4) in the rescaled frame as

$$\begin{aligned}
&\left(\frac{\sigma_1}{H_1} + \frac{\sigma_2}{H_2}\right)\bar{\mu}_1 + \frac{1}{\pi}\left(\frac{\sigma_1}{H_1} - \frac{\sigma_2}{H_2}\right)\int \bar{\mu}_1(\bar{\mathbf{y}})\frac{\partial \ln|\bar{\mathbf{x}} - \bar{\mathbf{y}}|}{\partial \mathbf{n}(\bar{\mathbf{y}})} d\bar{s}(\bar{\mathbf{y}}) \\
&- \left(\frac{K_1}{H_1} + \frac{K_2}{H_2}\right)\bar{\mu}_2 - \frac{1}{\pi}\left(\frac{K_1}{H_1} - \frac{K_2}{H_2}\right)\int \bar{\mu}_2(\bar{\mathbf{y}})\frac{\partial \ln|\bar{\mathbf{x}} - \bar{\mathbf{y}}|}{\partial \mathbf{n}(\bar{\mathbf{y}})} d\bar{s}(\bar{\mathbf{y}}) \\
&= 2\gamma\bar{\kappa} - \left(\frac{\sigma_1}{H_1} - \frac{\sigma_2}{H_2}\right)\frac{Q\bar{R}}{2\pi b}(2\ln\bar{R} + \ln|\bar{\mathbf{x}}|^2) + \left(\frac{K_1}{H_1} - \frac{K_2}{H_2}\right)\frac{I\bar{R}}{2\pi b}(2\ln\bar{R} + \ln|\bar{\mathbf{x}}|^2),
\end{aligned} \tag{A12}$$

and

$$\begin{aligned}
&- \left(\frac{K_1}{H_1} + \frac{K_2}{H_2}\right)\bar{\mu}_1 - \frac{1}{\pi}\left(\frac{K_1}{H_1} - \frac{K_2}{H_2}\right)\int \bar{\mu}_1(\bar{\mathbf{y}})\frac{\partial \ln|\bar{\mathbf{x}} - \bar{\mathbf{y}}|}{\partial \mathbf{n}(\bar{\mathbf{y}})} d\bar{s}(\bar{\mathbf{y}}) \\
&+ \left(\frac{M_1}{H_1} + \frac{M_2}{H_2}\right)\bar{\mu}_2 + \frac{1}{\pi}\left(\frac{M_1}{H_1} - \frac{M_2}{H_2}\right)\int \bar{\mu}_2(\bar{\mathbf{y}})\frac{\partial \ln|\bar{\mathbf{x}} - \bar{\mathbf{y}}|}{\partial \mathbf{n}(\bar{\mathbf{y}})} d\bar{s}(\bar{\mathbf{y}}) \\
&= \left(\frac{K_1}{H_1} - \frac{K_2}{H_2}\right)\frac{Q\bar{R}}{2\pi b}(2\ln\bar{R} + \ln|\bar{\mathbf{x}}|^2) - \left(\frac{M_1}{H_1} - \frac{M_2}{H_2}\right)\frac{I\bar{R}}{2\pi b}(2\ln\bar{R} + \ln|\bar{\mathbf{x}}|^2).
\end{aligned} \tag{A13}$$

Using Eq. (A5), we are able to compute the normal velocity in the rescaled frame

$$\bar{V}(\bar{\mathbf{x}}) = \frac{1}{2\pi\bar{R}}\int \bar{\mu}_{1\bar{s}}\frac{(\bar{\mathbf{x}}' - \bar{\mathbf{x}})^{\perp} \cdot \bar{\mathbf{n}}(\bar{\mathbf{x}})}{|\bar{\mathbf{x}}' - \bar{\mathbf{x}}|^2} d\bar{s}' + \frac{\bar{Q}}{2\pi b}\frac{\bar{\mathbf{x}} \cdot \bar{\mathbf{n}}}{|\bar{\mathbf{x}}|^2} - \frac{\bar{Q}}{2b\bar{A}(0)}\bar{\mathbf{x}} \cdot \bar{\mathbf{n}}, \tag{A14}$$

where $\bar{\mathbf{x}}^{\perp} = (\bar{x}_2, -\bar{x}_1)$. Then we evolve the interface in the scaled frame through

$$\frac{d\bar{\mathbf{x}}(\bar{t}, \theta)}{d\bar{t}} \cdot \mathbf{n} = \bar{V}(\bar{t}, \theta). \tag{A15}$$

### Appendix B: Second-order, mode-coupling perturbative analysis

In this Appendix, we develop a second-order, perturbative weakly nonlinear theory for our electrohydrodynamic problem. Our leading goal is to find a differential equation which describes the time evolution of the perturbation amplitudes $\delta_n(t)$, accurate to second-order $[O(\delta_n^2)]$. Therefore, we perform the same steps already presented in Sec. II to obtain the linear growth rate of the system. However, instead of keeping terms up to first-order in $\delta$, we extend the linear theory by keeping terms consistently up to second-order in $\delta$. Contrary to the usual linear stability analysis, which essentially provides information about the stability of the interface with respect to small perturbations, our second-order weakly nonlinear theory allows one to extract key information about the morphology of the interfacial patterns at the onset of nonlinearity. We seek to verify and strengthen the findings already obtained via our computational scheme (Figs. 2 – 6) by utilizing an alternative approach based on a second-order, perturbative strategy.

During the injection process, the initially slightly perturbed circular interface can become unstable, and deform, due to the interplay of viscous, capillary, and electric forces acting on the system. In our perturbative analysis, the perturbed shape of the fluid-fluid boundary is described by $\mathcal{R}(\theta, t) = R(t) + \delta(\theta, t)$. Recall that the velocity $\mathbf{v}_j$ and current density $\mathbf{J}_j$ fields are irrotational in the bulk. Therefore, we can state our problem in terms of the Laplacian velocity and current density potentials [35, 36, 59]

$$\phi_j(r, \theta) = -\frac{Q}{2\pi b} \log\left(\frac{r}{R}\right) + \sum_{n\neq 0} \phi_{jn}(t) \left(\frac{r}{R}\right)^{(-1)^{(j+1)}|n|} e^{in\theta}, \tag{B1}$$

and

$$\psi_j(r, \theta) = -\frac{I}{2\pi b} \log\left(\frac{r}{R}\right) + \sum_{n\neq 0} \psi_{jn}(t) \left(\frac{r}{R}\right)^{(-1)^{(j+1)}|n|} e^{in\theta}, \tag{B2}$$

respectively.

Within this perturbative framing, we use the kinematic boundary conditions to express the potentials $\phi_j(t)$ and $\psi_j(t)$ in terms of the perturbation amplitudes $\delta_n(t)$, and their time derivatives $\dot{\delta}_n(t) = d\delta_n(t)/dt$. Next, we substitute the resulting relations, the pressure jump condition, and continuity of electric potential into Darcy's law. Likewise, we also substitute these relations into the total current density. Then, since $\mathbf{v}_j$ and $\mathbf{J}_j$ are coupled, we can insert one of them into the other, obtaining a single expression in terms of $\delta_n(t)$ and $\dot{\delta}_n(t)$. In contrast to what has been done in Sec. II to obtain the linear growth rate of the system, here we extend the linear theory by keeping terms consistently up to second-order in $\delta$. By doing this, we obtain the *weakly nonlinear* equation of motion for the perturbation amplitudes (for $n \neq 0$)

$$\dot{\delta}_n = \lambda(n)\delta_n + \sum_{n'\neq 0} \left[F(n, n') + \lambda(n')G(n, n')\right] \delta_{n'}\delta_{n-n'}. \tag{B3}$$

In Eq. (B3), $\lambda(n)$ is the linear growth rate given by Eq. (1), and the second-order mode-coupling terms appearing on the right-hand side are given by

$$\begin{aligned} F(n, n') = \frac{|n|}{R} \Bigg\{ & \frac{Q}{2\pi b R^2} \left[ A\left[\frac{1}{2} - \mathrm{sgn}(nn')\right] + (DA - E)|n'|[1 - \mathrm{sgn}(nn')] \right] - \frac{\gamma}{R^3} \Bigg[ B\left[1 - \frac{n'}{2}(3n' + n)\right] \\ & + (f + BD)|n'|(n'^2 - 1)[1 - \mathrm{sgn}(nn')] \Bigg] + \frac{IC}{\pi b R^2} \left[ D|n'|[1 - \mathrm{sgn}(nn')] - \frac{1}{2} \right] \Bigg\}, \end{aligned} \tag{B4}$$

and

$$G(n, n') = \frac{1}{R} \left\{ A|n|[1 - \mathrm{sgn}(nn')] - 1 \right\}, \tag{B5}$$

where

$$D = \frac{K_1^2 - K_2^2 - (\sigma_1 - \sigma_2)(M_1 + M_2)}{(K_1 + K_2)^2 - (\sigma_1 + \sigma_2)(M_1 + M_2)}, \tag{B6}$$

$$E = \frac{(K_1 - K_2)^2 - (\sigma_1 - \sigma_2)(M_1 - M_2)}{(K_1 + K_2)^2 - (\sigma_1 + \sigma_2)(M_1 + M_2)}, \tag{B7}$$

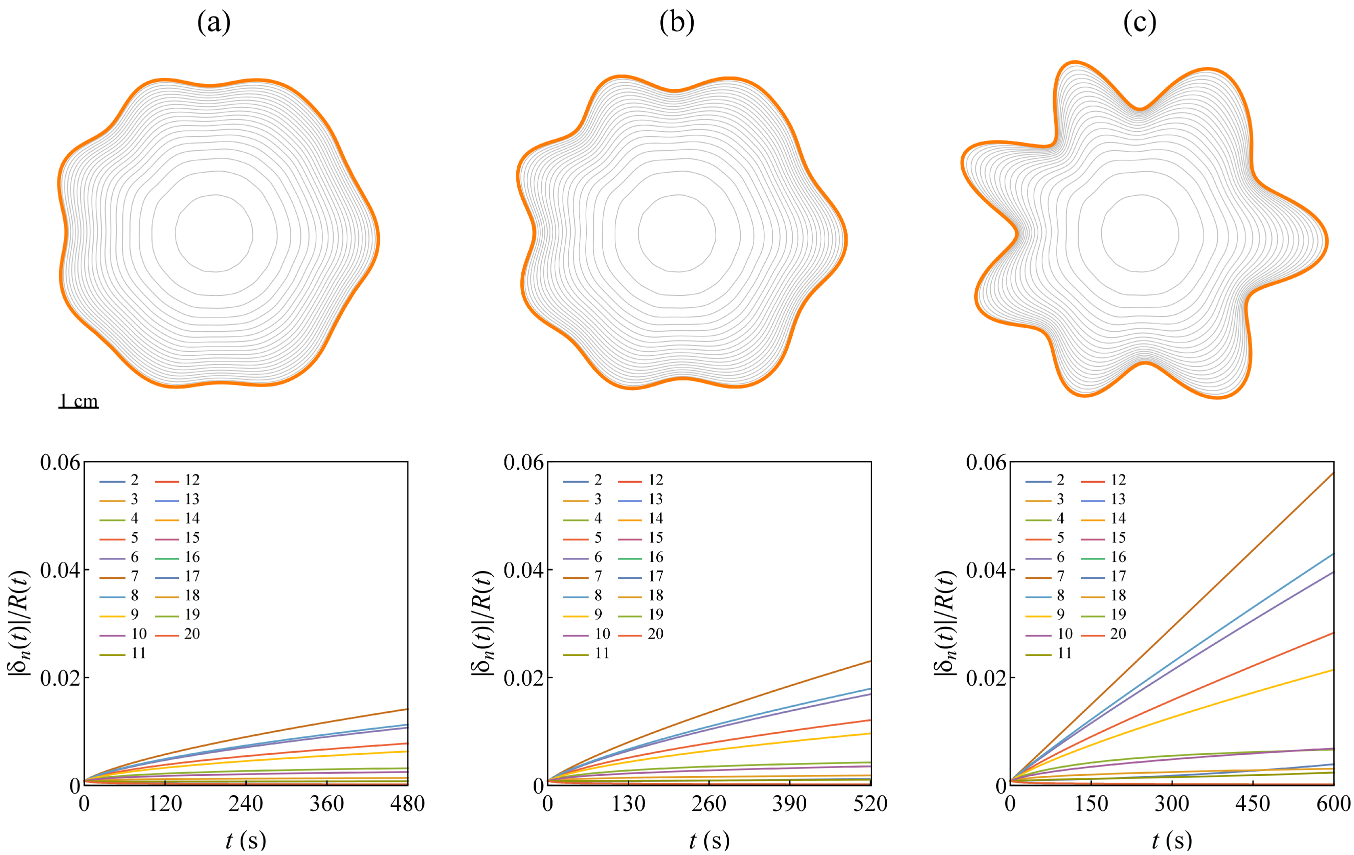


FIG. 7. Weakly nonlinear time evolution of the expanding interfacial patterns generated by utilizing the controlling protocol for $n_{\max} = 7$, and three injection rates $Q(t) = \alpha Q_{\rm crit}(t)$: (a) $\alpha = 0.25$, (b) $\alpha = 0.23$, and (c) $\alpha = 0.2$. Here we include modes $2 \leq n \leq 20$ and a random initial phase. The corresponding time evolution of the rescaled perturbation mode amplitudes $|\delta_n(t)|/R(t)$ are shown in the bottom panels. The final times used are (a) $t_f = 480$ s, and (b) $t_f = 600$ s, and the remaining physical parameters are listed in Table I.

$$f = \frac{M_1 K_2^2 - M_2 K_1^2 + (\sigma_1 - \sigma_2) M_1 M_2}{(K_1 + K_2)^2 - (\sigma_1 + \sigma_2)(M_1 + M_2)}, \tag{B8}$$

and the sgn function equals $\pm 1$ according to the sign of its argument.

Expressions (B3)-(B8) are the second-order mode-coupling equations describing the time evolution of the interfacial shape during a radial injection process in a Hele-Shaw cell, taking into account electro-osmotic effects. Note that after neglecting the second-order terms in Eq. (B3), one verifies that Eqs. (B3)-(B8) agree with the simpler linear (first-order) expression previously derived in Sec. II. In the absence of electro-osmotic effects ($K_1 = K_2 = 0$), our second-order results also reproduce the second-order expressions obtained in Ref. [59] which analyzed radial injection in a Hele-Shaw cell.

In order to plot the weakly nonlinear temporal evolution of the interfaces, we first consider the nonlinear coupling of all the Fourier modes in the interval $2 \leq n \leq 20$, and rewrite the net interfacial perturbation $\delta(\theta, t)$ in terms of the real-valued cosine $a_n(t) = \delta_n(t) + \delta_{-n}(t)$, and sine $b_n(t) = i[\delta_n(t) - \delta_{-n}(t)]$ amplitudes. Once this is done, the shape of the evolving interface can be easily acquired through

$$\mathcal{R}(\theta, t) = R(t) + \delta_0 + \sum_{n=2}^{20} [a_n(t)\cos(n\theta) + b_n(t)\sin(n\theta)], \tag{B9}$$

where $\delta_0 = -(1/2R)\sum_{n=1}^{\infty}\left[|\delta_n(t)|^2 + |\delta_{-n}(t)|^2\right]$ [59] is an intrinsically nonlinear constraint related to the inner fluid mass conservation. The time evolution of the mode amplitudes $a_n(t)$ and $b_n(t)$ can be obtained by numerically solving the corresponding coupled nonlinear differential equations

$$\dot{a}_n = \lambda(n)a_n + \frac{1}{2}\sum_{n'>0}\left\{W_0(n,-n')a_{n'}a_{n+n'} + W_0(n,n')a_{n'}a_{n-n'} + W_0(n,-n')b_{n'}b_{n+n'} - W_0(n,n')b_{n'}b_{n-n'}\right\}, \tag{B10}$$

and

$$\dot{b}_n = \lambda(n)b_n + \frac{1}{2}\sum_{n'>0}\left\{W_0(n,-n')a_{n'}b_{n+n'} + W_0(n,n')a_{n'}b_{n-n'} - W_0(n,-n')b_{n'}a_{n+n'} + W_0(n,n')b_{n'}a_{n-n'}\right\}, \tag{B11}$$

where

$$W_0(n,n') = F(n,n') + \lambda(n')G(n,n'). \tag{B12}$$

Eqs. (B10) and (B11) are obtained by utilizing Eq. (B3). Furthermore, we set the initial ($t = 0$) amplitude of all perturbation modes as $R_0/600$. To make the initial conditions as general as possible, we consider the action of random phases attributed to each participating sine and cosine mode. This guarantees that the interfacial behaviors we detect are spontaneously generated by the weakly nonlinear dynamics and not by artificially imposing large initial amplitudes for the modes.

In Fig. 7, we utilize our second-order, weakly nonlinear perturbative approach to verify the efficiency of our controlling protocol during the onset of nonlinearities. In the top panels of Fig. 7, we plot the weakly nonlinear evolution of the interface employing the controlling current Eq. (5) for $n_{\max} = 7$ and injection rates $Q(t) = \alpha Q_{\rm crit}(t)$, with (a) $\alpha = 0.25$, (b) $\alpha = 0.23$, and (c) $\alpha = 0.2$. The final time $t_f$ is defined as the time at which the interface unperturbed radius has reached the same magnitude [namely, $R(t = t_f) \approx 4$ cm] for each $Q(t)$ employed. This is done in order to make the generated patterns to have the same size at $t = t_f$. In these circumstances, the final times are taken as (a) $t_f = 480$ s, (b) $t_f = 522$ s, and (c) $t_f = 600$ s. In the bottom panels we show the corresponding time evolution of the rescaled perturbation amplitudes $|\delta_n(t)|/R(t)$.

By analyzing the top panels of Fig. 7, we observe that the three patterns evolve to 7-fold fingered structures, regardless of the injection rate employed. In addition, note that although all the patterns have the same number of fingers and are generated employing precisely the same initial conditions and physical parameters (see Table I), we observe that lower injection rates lead to the formation of increasingly disturbed patterns. This effect can also be perceived and appropriately quantified by noting that the magnitudes of the rescaled perturbation amplitudes $|\delta_n(t_f)|/R(t_f)$ in the bottom panel of Fig. 7(c) are larger than the magnitudes found in the bottom panels of Figs. 7(a) and 7(b). These weakly nonlinear findings further support some of the results already presented in Sec. IV.


[1] P. G. Saffman and G. I. Taylor, The penetration of a fluid into a porous medium or Hele-Shaw cell containing a more viscous liquid, Proc. R. Soc. London Ser. A **245**, 312 (1958).
[2] L. Paterson, Radial fingering in a Hele-Shaw cell, J. Fluid Mech. **113**, 513 (1981).
[3] G. M. Homsy, Viscous fingering in porous media, Annu. Rev. Fluid Mech. **19**, 271 (1987).
[4] K. V. McCloud and J. V. Maher, Experimental perturbations to Saffman-Taylor flow, Phys. Rep. **260**, 139 (1995).
[5] J. Casademunt, Viscous fingering as a paradigm of interfacial pattern formation: Recent results and new challenges, Chaos **14**, 809 (2004).
[6] S. B. Gorell and G. M. Homsy, A theory of the optimal policy of oil recovery by secondary displacement processes, SIAM J. Appl. Math. **43**, 79 (1983).
[7] J. P. Stokes, D. A. Weitz, J. P. Gollub, A. Dougherty, M. O. Robbins, P. M. Chaikin, and H. M. Lindsay, Interfacial stability of immiscible displacement in a porous medium, Phys. Rev. Lett. **57**, 1718 (1986).
[8] D. Derks, A. Lindner, C. Creton, and D. Bonn, Cohesive failure of thin layers of soft model adhesives under tension, J. Appl. Phys. **93**, 1557 (2003).
[9] J. Nase, D. Derks, and A. Lindner, Dynamic evolution of fingering patterns in a lifted Hele-Shaw cell, Phys. Fluids **23**, 123101 (2011).
[10] P. H. A. Anjos, E. O. Dias, L. Dias, and J. A. Miranda, Adhesion force in fluids: Effects of fingering, wetting, and viscous normal stresses, Phys. Rev. E **91**, 013003 (2015).
[11] B. Jha, L. Cueto-Felgueroso, and R. Juanes, Fluid mixing from viscous fingering, Phys. Rev. Lett. **106**, 194502 (2011).
[12] T. T. Al-Housseiny and H. A. Stone, Controlling viscous fingering in tapered Hele-Shaw cells, Phys. Fluids **25**, 092102 (2013).
[13] G. Bongrand and P. A. Tsai, Manipulation of viscous fingering in a radially tapered cell geometry, Phys. Rev. E **97**, 061101 (R) (2018).
[14] P. H. A. Anjos, E. O. Dias, and J. A. Miranda, Fingering instability transition in radially tapered Hele-Shaw cells: Insights at the onset of nonlinear effects, Phys. Rev. Fluids **3**, 124004 (2018).

[15] L. C. Morrow, T. J. Monorey, and S. W. McCue, Numerical investigation of controlling interfacial instabilities in non-standard Hele-Shaw configurations, J. Fluid Mech. **877**, 1063 (2019).
[16] E. O. Dias and J. A. Miranda, Taper-induced control of viscous fingering in variable-gap Hele-Shaw flows, Phys. Rev. E **87**, 053015 (2013).
[17] E. O. Dias and J. A. Miranda, Control of centrifugally driven fingering in a tapered Hele-Shaw cell, Phys. Rev. E **87**, 053014 (2013).
[18] D. Pihler-Puzović, G. G. Peng, J. R. Lister, M. Heil, and A. Juel, Viscous fingering in a radial elastic-walled Hele-Shaw cell, J. Fluid Mech. **849**, 163 (2018).
[19] S. Li, J. S. Lowengrub, J. Fontana, and P. Palffy-Muhoray, Control of viscous fingering patterns in a radial Hele-Shaw cell, Phys. Rev. Lett. **102**, 174501 (2009).
[20] E. O. Dias and J. A. Miranda, Control of radial fingering patterns: A weakly nonlinear approach, Phys. Rev. E **81**, 016312 (2010).
[21] E. O. Dias, F. Parisio, and J. A. Miranda, Suppression of viscous fluid fingering: A piecewise-constant injection process, Phys. Rev. E **82**, 067301 (2010).
[22] E. O. Dias, E. Alvarez-Lacalle, M. S. Carvalho, and J. A. Miranda, Minimization of viscous fluid fingering: A variational scheme for optimal flow rates, Phys. Rev. Lett. **109**, 144502 (2012).
[23] Í. M. Coutinho and J. A. Miranda, Control of viscous fingering through variable injection rates and time-dependent viscosity fluids: Beyond the linear regime, Phys. Rev. E **102**, 063102 (2020).
[24] T. H. Beeson-Jones and A. W. Woods, Control of viscous instability by variation of injection rate in a fluid with time-dependent rheology, J. Fluid Mech. **829**, 214 (2017).
[25] E. O. Dias, Viscous-fingering minimization in uniform three-dimensional porous media, Phys. Rev. E **88**, 063007 (2013).
[26] J. V. Fontana, E. O. Dias, and J. A. Miranda, Controlling and minimizing fingering instabilities in non-Newtonian fluids, Phys. Rev. E **89**, 013016 (2014).
[27] C. Batista, E. O. Dias, and J. A. Miranda, Hamiltonian formulation towards minimization of viscous fluid fingering, Phys. Rev. E **94**, 013109 (2016).
[28] P. H. A. Anjos, M. Zhao, J. Lowengrub, W. Bao, and S. Li, Controlling fingering instabilities in Hele-Shaw flows in the presence of wetting film effects, Phys. Rev. E **103**, 063105 (2021).
[29] S. S. S. Cardoso and A. W. Woods, The formation of drops through viscous instability, J. Fluid Mech. **289**, 351 (1995).
[30] C. Vaquero-Stainer, M. Heil, A. Juel, and D. Pihler-Puzović, Self-similar and disordered front propagation in a radial Hele-Shaw channel with time-varying cell depth, Phys. Rev. Fluids **4**, 064002 (2019).
[31] Z. Zheng, H. Kim, and H. A. Stone, Controlling viscous fingering using time-dependent strategies, Phys. Rev. Lett. **115**, 174501 (2015).
[32] E. O. Dias and J. A. Miranda, Variational scheme towards an optimal lifting drive in fluid adhesion, Phys. Rev. E **86**, 046322 (2012).
[33] M. Zhao, X. Li, W. Ying, A. Belmonte, J. Lowengrub, and S. Li, Computation of a shrinking interface in a Hele-Shaw cell, SIAM J. Sci. Comput. **40**, B1206 (2018).
[34] M. Zhao, Z. Niroobakhsh, J. Lowengrub, and S. Li, Nonlinear limiting dynamics of a shrinking interface in a Hele-Shaw cell, J. Fluid Mech. **910**, A41 (2021).
[35] M. Mirzadeh and M. Z. Bazant, Electrokinetic control of viscous fingering, Phys. Rev. Lett. **119**, 174501 (2017).
[36] T. Gao, M. Mirzadeh, P. Bai, K. M. Conforti, and M. Z. Bazant, Active control of viscous fingering using electric fields, Nat. Commun. **10**, 4002 (2019).
[37] B. J. Kirby and E. F. Hasselbrink, Zeta potential of microfluidic substrates: 1. Theory, experimental techniques, and effects on separations, Electrophoresis **25**, 187 (2004).
[38] R. J. Hunter, *Zeta Potential in Colloid Science: Principles and Applications*, 3rd ed. (Academic Press, New York, 1988).
[39] R. J. Hunter, *Foundations of Colloid Science*. (Oxford University Press, New York, 2001).
[40] M. Mirzadeh, T. Zhou, M. A. Amooie, D. Fraggedakis, T. R. Ferguson, and M. Z. Bazant, Vortices of electro-osmotic flow in heterogeneous porous media, Phys. Rev. Fluids **5**, 103701 (2020).
[41] S. Li, J. S. Lowengrub, and P. H. Leo, A rescaling scheme with application to the long-time simulation of viscous fingering in a Hele-Shaw cell, J. Comput. Phys. **225**, 554 (2007).
[42] M. Zhao, W. Yin, J. Lowengrub, and S. Li, An Efficient adaptive rescaling scheme for computing moving interface problems, Commun. Compt. Phys. **21**, 679 (2017).
[43] M. Zhao, P. H. A. Anjos, J. Lowengrub, W. Ying, and S. Li, Numerical study on viscous fingering using electric fields in a Hele-Shaw cell, arXiv:2201.05956.
[44] Supplementary Movies 1-4 present the evolution of the patterns displayed in Figs. 3(c)-(f), respectively.
[45] P. H. A. Anjos, S. A. Lira, and J. A. Miranda, Fingering patterns in magnetic fluids: Perturbative solutions and the stability of exact stationary shapes, Phys. Rev. Fluids **3**, 044002 (2018).
[46] A. O. Tsebers and M. M. Maiorov, Magnetostatic instabilities in plane layers of magnetizable fluids, Magnetohydrodynamics **16**, 21 (1980).
[47] A. O. Cebers, Dynamics of magnetostatic instabilities, Magnetohydrodynamics **17**, 113 (1981).
[48] S. A. Langer, R. E. Goldstein, and D. P. Jackson, Dynamics of labyrinthine pattern formation in magnetic fluids, Phys. Rev. A **46**, 4894 (1992).
[49] D. P. Jackson, R. E. Goldstein, and A. O. Cebers, Hydrodynamics of fingering instabilities in dipolar fluids, Phys. Rev. E **50**, 298 (1994).

[50] J. Kent-Dobias and A. J. Bernoff, Energy-driven pattern formation in planar dipole-dipole systems in the presence of weak noise, Phys. Rev. E **91**, 032919 (2015).
[51] C.-Y. Chen, Y.-S. Yang, and J. A. Miranda, Miscible ferrofluid patterns in a radial magnetic field, Phys. Rev. E **80**, 016314 (2009).
[52] C.-Y. Chen, W.-L. Wu, and J. A. Miranda, Magnetically induced spreading and pattern selection in thin ferrofluid drops, Phys. Rev. E **82**, 056321 (2010).
[53] R. M. Oliveira, J. A. Miranda, and E. S. G. Leandro, Ferrofluid patterns in a radial magnetic field: Linear stability, nonlinear dynamics, and exact solutions, Phys. Rev. E **77**, 016304 (2008).
[54] S. A. Lira, J. A. Miranda, and R. M. Oliveira, Field-induced patterns in confined magnetorheological fluids, Phys. Rev. E **81**, 046303 (2010).
[55] Z. Yu and I. C. Christov, Tuning a magnetic field to generate spinning ferrofluid droplets with controllable speed via nonlinear periodic interfacial waves, Phys. Rev. E **103**, 013103 (2021).
[56] R. Kress, *Linear Integral Equations*, (Berlin: Springer **82** 1989).
[57] Y. Saad and M. H. Schultz, GMRES: A generalized minimal residual algorithm for solving nonsymmetric linear systems, SIAM J. Sci. Stat. Comput. **7**, 856 (1986).
[58] A. Greenbaum, L. Greengard, and G. B. McFadden, Laplace's equation and the Dirichlet-Nuemann map in multiply connected domains, J. Comput. Phys. **105**, 267 (1993).
[59] J. A. Miranda and M. Widom, Radial fingering in a Hele-Shaw cell: A weakly nonlinear analysis, Physica D **120**, 315 (1998).